Responses of Cloud-Radiative Forcing to Strong El Niño Events over the Western Pacific Warm Pool as Simulated by CAMS-CSM

Baichao ZHANG[1], Zhun GUO[2,3], Xiaolong CHEN[3,4], Tianjun ZHOU[3,4,5*], Xinyao RONG[6], and Jian LI[6]

1 *Nanjing University of Information Science & Technology*, *Nanjing* 210044
2 *Climate Change Research Center*, *Chinese Academy of Sciences*, *Beijing* 100029
3 *State Key Laboratory of Numerical Modeling for Atmospheric Sciences and Geophysical Fluid Dynamics*, *Institute of Atmospheric Physics*, *Chinese Academy of Sciences*, *Beijing* 100029
4 *CAS Center for Excellence in Tibetan Plateau Earth Sciences*, *Chinese Academy of Sciences (CAS)*, *Beijing* 100101
5 *University of Chinese Academy of Sciences*, *Beijing* 100049
6 *Chinese Academy of Meteorological Sciences*, *China Meteorological Administration*, *Beijing* 100081

(Received September 30, 2019; in final form March 2, 2020)

ABSTRACT

Cloud-radiative forcing (CRF) at the top of the atmosphere (TOA) over the western Pacific warm pool (WP) shows unique characteristics in response to El Niño events. In this region, the responses of CRF to El Niño events have been a useful metric for evaluating climate models. Satellite data are used to analyze the CRF anomalies to El Niño events simulated by the new and old versions of the Climate System Model of the Chinese Academy of Meteorological Sciences (CAMS-CSM), which has participated in the Atmospheric Model Intercomparison Project (AMIP). Here, simulations for super El Niño years, El Niño years, and normal years are compared with observations. The results show that the mean values of both longwave CRF (LWCRF) and shortwave CRF (SWCRF) in CAMS-CSM are weaker than the observations for each category of El Niño events. Compared with the old version of CAMS-CSM, the decrease in LWCRF during El Niño events is well simulated by the new version of CAMS-CSM. However, both new and old models cannot reproduce the anomalous SWCRF in El Niño events. The biases in the CRF response to El Niño events are attributed to the biases in the cloud vertical structure because of a weaker crash of the Walker circulation in CAMS-CSM. Due to the modification of the conversion rate from cloud droplets to raindrops in the cumulus convection scheme, the new version of CAMS-CSM has better CRF skills in normal years, but biases in El Niño events still exist in the new version. Improving the response of the Walker circulation to El Niño events is key to higher skills in simulating the cloud radiative responses.

Key words: cloud-radiative forcing (CRF), El Niño, model evaluation, warm pool (WP), western Pacific

Citation: Zhang, B. C., Z. Guo, X. L. Chen, et al., 2020: Responses of cloud-radiative forcing to strong El Niño events over the western Pacific warm pool as simulated by CAMS-CSM. *J. Meteor. Res.*, **34**(3), 499–514, doi: 10.1007/s13351-020-9161-3.

1. Introduction

Deep cumulus and cirrus clouds, which are associated with updrafts of the Walker circulation, cover a large area of the western Pacific warm pool (WP). This area attracts worldwide attention because of its unique features in cloud-radiative forcing (CRF) in response to El Niño events. During normal years, strong updrafts of the Walker circulation lead to deep convective clouds wrapping over the WP, increasing the shortwave CRF (SWCRF) and longwave CRF (LWCRF) at the top of the atmosphere (TOA). As an offset between negative SWCRF and positive LWCRF, the net CRF (NETCRF) is approximately zero (Kiehl and Ramanathan, 1990; Hartmann et al., 1992; Zhang et al., 1995; Chen et al., 2000; Harrop and Hartmann, 2015). During El Niño events, however, the zonal gradient of the sea surface temperature (SST) in the tropical Pacific (TP) weakens, and the Walker circulation could even completely crash in some extreme events (e.g., 1998). The weakened updraft over

Supported by the Ministry of Science and Technology of China (2017YFA0604004) and National Natural Science Foundation of China (41775102, 41420104006, and 41661144009).

*Corresponding author: zhoutj@lasg.iap.ac.cn.

the WP then leads to a shallower cloud top than that during normal years, producing stronger negative NETCRF (Cess et al., 2001a, b; Burls and Fedorov, 2014; Kiran et al., 2015; Wang and Su, 2015; Wall et al., 2018). Because of the unique cloud vertical structure and the different features of CRF between normal years and El Niño events, CRF over the WP has been regarded as a useful metric for evaluating the climate models (Lu et al., 2004; Wu et al., 2010, 2011; Guo and Zhou, 2012).

Climate models are widely used to simulate the current climate and predict future changes. Accurate simulation of the cloud structure is a necessary condition for reliable future projections. CRF, as a useful index for quantifying cloud–climate effects, is poorly simulated by most models because of the complex radiative properties of clouds. Different CMIP5 (Coupled Model Intercomparison Project Phase 5) models have different biases in the simulated CRF in the TP, and the models with a more realistic dynamic framework have better CRF simulation skills (Webb et al., 2001, 2006; Soden and Held, 2006; Williams and Webb, 2009). Thus, improving the simulation of the CRF process is an effective means to improve the performance of the CMIP6 models.

The Climate System Model of the Chinese Academy of Meteorological Sciences (CAMS-CSM) has been officially planned to take part in the CMIP6. The model shows a promising ability to simulate the EASM (East Asian summer monsoon) variability and the ENSO–EASM relationship (Rong et al., 2018). CAMS-CSM can generally reproduce the features of SWCRF and LWCRF, but it underestimates the thermodynamic damping and thermocline feedbacks caused by the biases of the SWCRF feedbacks in ENSO simulations (Chen et al., 2019; Hua and Chen, 2019; Lu and Ren, 2019). A recent study shows that the shortwave radiation flux and the corresponding total cloud cover simulated by CAMS-CSM are unrealistic in ENSO events (Hua et al., 2019), but the reason remains to be clarified.

Compared with the CRF in the pre-industrial control simulation (piControl), the Atmospheric Model Intercomparison Project (AMIP) simulation driven by the observed SST exhibits a better performance in simulating the magnitude and spatial distribution for both normal and ENSO years (Chen et al., 2019). A more in-depth analysis of the responses of CRF to El Niño events in the AMIP simulation will provide useful references for better understating the bias of the fully coupled model. In the present study, we use the AMIP results from CAMS-CSM to assess the simulation skills of WP CRF responses to El Niño events. The cause of the CRF simulation biases will also be investigated by comparing the old and new versions of CAMS-CSM, as some improvements related to cloud microphysics and radiation have been implemented in the new version.

The remainder of this paper is organized as follows. Section 2 provides a brief introduction of the data, model, and methods in this study. In Section 3, we assess the simulation skills of CRF in the CAMS-CSM AMIP runs using old and new versions of the model, and determine the cause of the simulated biases between the observations and the CAMS-CSM results. We then discuss how the modification in the new version affects the simulation skills of cloud radiation. Finally, Section 4 summarizes the results of the study.

2. Data, model, and methods

2.1 *Data*

(1) The observed monthly cloud fraction and grid-mean integrated cloud water path (CWP) are derived from the International Satellite Cloud Climatology Project (ISCCP) D2 from July 1983 to June 2007 with a 2.5° × 2.5° latitude–longitude resolution (Rossow and Schiffer, 1991).

(2) Three observed radiation datasets are used. (i) Monthly radiation at the TOA provided by Clouds and the Earth's Radiant Energy System (CERES) during 2001 to 2005 at a 1° × 1° latitude–longitude resolution (Wielicki et al., 1996); (ii) monthly radiation data derived from ISCCP-FD (Flux Data) on a 2.5° grid from 1984 to 2005 (Zhang et al., 2004); and (iii) monthly radiation data derived from the CERES-TRMM (Tropical Rainfall Measuring Mission) in 1998 at a spatial resolution of 2.5°, which are widely used to analyze the super El Niño events of 1998 (Wong et al., 2000).

(3) Wind data are derived from the ERA-Interim atmospheric reanalysis monthly data from 1979 to 2005 on a 1.5° × 1.5° latitude–longitude resolution at standard pressure levels. The spatial resolution of the dataset is approximately 80 km (T255 spectral), with 60 vertical levels from the surface up to 0.1 hPa (Simmons et al., 2006).

All the data are interpolated to 1° × 1° latitude–longitude grids based on bilinear interpolation in this study. Following Lu et al. (2004), we used the mean of the first four months (January, February, March, and April; JFMA for short) in a year to define the strongest period of the El Niño events.

2.2 *Model and experiments*

The CAMS-CSM is a global primitive-equation model

based on the ECHAM5 (ECmwf-HAMburg v5.4) atmospheric model developed by the Max Planck Institute for Meteorology and has 31 vertical levels with a top at 10 hPa (Roeckner et al., 2003). The Tiedtke (1989) mass flux scheme, which includes modifications for penetrative convection according to Nordeng (1994), is applied for cumulus convection parameterization. The convective cloud scheme was developed by Tiedtke (1993). The stratiform cloud scheme consists of a cloud microphysical scheme (Lohmann and Roeckner, 1996) and a cloud cover scheme, which diagnostically calculate the cloud fraction as a function of relative humidity (Sundqvist, 1978). The subgrid cloud formation is diagnosed as follows: clouds occur where the relative humidity exceeds the prescribed threshold of 85% at the top of the planetary boundary layer (PBL) and increases linearly to the surface layer (99%). When penetrative convection occurs, the threshold decreases further to a minimum value of 0.5 near the tropopause. The radiation scheme adopted in the model was developed by Zhang et al. (2003, 2006a, b) and can improve the simulation of SWCRF over East Asia. More details of CAMS-CSM can be found in Rong et al. (2018).

The AMIP run of the two versions of CAMS-CSM is the same as that used for the historical forcing data during 1900–2013, including monthly observations of SST, solar forcing, greenhouse gases (CO_2, CH_4, N_2O, CFC-12, and equivalent CFC-11 that summarizes the effects of all 39 other gases), and anthropogenic aerosols. The differences between the new version and the old version of CAMS-CSM include 1) a modification of the conversion rate from cloud droplets to raindrops in the cumulus convection scheme and 2) addition of an effective solar zenith angle scheme, which accounts for the curvature of the atmosphere and its effect on the length of the optical path of direct solar beam with respect to a plane-parallel atmosphere. In this study, we use the mean of three members of the new version to indicate the new version of CAMS-CSM.

2.3 *CRF*

SWCRF, LWCRF, and NETCRF at the TOA are defined as follows:

$$\mathrm{SWCRF} = R_\mathrm{c} - R, \tag{1}$$

$$\mathrm{LWCRF} = F_\mathrm{c} - F, \tag{2}$$

$$\mathrm{NETCRF} = \mathrm{SWCRF} + \mathrm{LWCRF}, \tag{3}$$

where R denotes all-sky reflected SW at the TOA, R_c represents clear-sky reflected SW, F is all-sky reflected LW at the TOA, and F_c denotes clear-sky reflected LW (Harrison et al., 1990).

We consider the radiation ratio N as follows (Lu et al., 2004):

$$N = -\mathrm{SWCRF}/\mathrm{LWCRF}. \tag{4}$$

If SWCRF cooling dominates, both NETCRF < 0 and $N > 1$ indicate that CRF cools the atmosphere; if LWCRF heating dominates, NETCRF > 0 and $N < 1$ show that CRF heats the atmosphere; and if NETCRF ≈ 0 and $N \approx 1$, the influences of LWCRF and SWCRF are nearly offset.

2.4 *Classification of the El Niño year*

We used the Niño3.4 index (5°N–5°S, 120°–170°W) from the NOAA website (https://www.esrl.noaa.gov/psd/gcos_wgsp/Timeseries/Data/nino34.long.anom.data), and the warm and cold episodes in the TP are determined with a threshold of ± 0.5°C of the Niño3.4 index. El Niño events are defined by a threshold of +1.0°C, while the threshold is +2.0°C for super El Niño events. When more than one month has a Niño3.4 index higher than +1.0°C from November to April, the year is defined as an El Niño year; when the Niño3.4 index is higher than +2.0°C, the year is defined as a super El Niño year. The El Niño events during 1979–2005 are listed in Table 1, including 5 El Niño and 2 super El Niño events. In this study, the super El Niño years are used to indicate El Niño because of its strong anomaly. However, there are only two super El Niño years; to exclude some specific features, we provide the results of five El Niño years to give an auxiliary illustration of the El Niño attributes.

2.5 *Identification of cloud vertical structure*

The relationship between N and NETCRF reflects the connection of the CRF with cloud vertical structure, such as the cloud top and cloud optical thickness (Cess et al., 2001a). Both the cloud fraction and the cloud optical thickness make positive contributions to the CRF. The contribution is linear for the cloud fraction but nonlinear

Table 1. Classification of the 1979–2005 years into super El Niño, El Niño, and normal years

Type	Super El Niño	El Niño	Normal
Year	1983, 1998	1987, 1988, 1992,1995, 2003	1979, 1980, 1981, 1982, 1984, 1985, 1986, 1989, 1990, 1991, 1993, 1994, 1996, 1997, 1999, 2000, 2001, 2002, 2004, 2005

for the cloud optical thickness. A schematic diagram of the scatter plot of N versus NETCRF is shown in Fig. 1. The blue and red lines and dots are clouds with different cloud top heights. If the cloud optical thickness is small, LWCRF dominates, which is represented by the dots in quadrant 4. When the cloud optical depth increases (arrows in blue and red), both SWCRF and LWCRF simultaneously increase, but SWCRF dominates in the process and causes an NETCRF decrease and the dots move to quadrant 2. The dots in quadrant 4 represent cirrus clouds with a small cloud optical thickness, while the dots in quadrant 2 represent deep convective clouds. The slope of the line reflects the cloud top. The line slope is steeper (red line) for low-top clouds than for high-top clouds (blue line) because N increases more quickly with the cloud optical thickness in low-top clouds due to the small LWCRF.

The above method can capture the characteristics of cloud vertical structure, including the cloud top and the cloud optical thickness (Potter and Cess, 2004). Because the outputs of the model do not include the cloud vertical structure, we used this method to analyze the three-dimensional structure of the cloud.

3. Results

3.1 *Evaluation of simulated tropical CRF*

The CAMS-CSM performance in all-year mean cloud radiative fluxes at the TOA is first evaluated. Figures 2 and 3 show the horizontal distributions of LWCRF and SWCRF, respectively, in two versions of CAMS-CSM and the ISCCP and CERES satellite products. LWCRF in the ISCCP and CERES exhibits maximum centers over the western Pacific WP region (5°S–5°N, 140°–165°E), Maritime Continent, and along the convergence zones; and minimum centers over the subtropical stratocumulus regimes. The SWCRF pattern is nearly a mirror image of the LWCRF pattern (Figs. 3a, d vs. Figs. 2a, d). Therefore, there is an expected cancellation between SWCRF and LWCRF over the western Pacific WP region (Kiehl and Ramanathan, 1990).

However, this balance between SWCRF and LWCRF over the TP is destroyed by the Walker circulation responses during winter and spring of El Niño years (Cess et al., 2001a). The cold SST anomalies in the western Pacific WP during El Niño years lead to suppressed convection and a lower cloud top and lower cloud amount, reducing both SWCRF and LWCRF (Figs. 3c, f vs. Figs. 2c, f). The SWCRF anomalies overwhelm LWCRF in the NETCRF budget over the WP.

The spatial patterns of the all-year mean LWCRF and SWCRF simulated by CAMS-CSM resemble those of satellite data to a large extent, except for the weaker simulated strength of CRF over the Maritime Continent. For example, the TP (10°S–10°N, 140°E–90°W) mean LWCRF in normal years is 23 W m^{-2} in the old version of CAMS-CSM, in comparison to less than 33 W m^{-2} in ISCCP and 34 W m^{-2} in CERES. LWCRF in the new

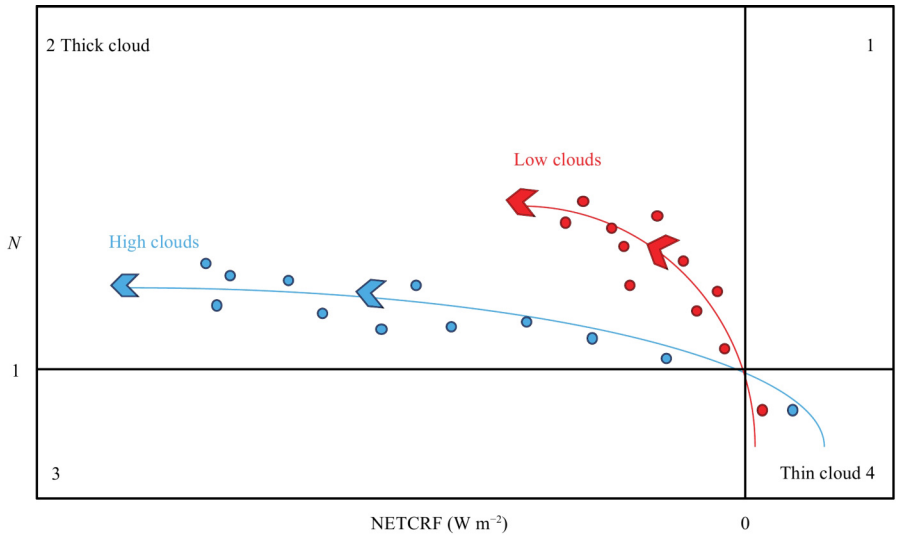

Fig. 1. Schematic diagram of the scatter plot for N vs. NETCRF. The numbers 1, 2, 3, and 4 indicate the different quadrants, and the vertical and horizontal lines indicate N = 1 and NETCRF = 0, which means an expected cancellation between SWCRF and LWCRF, respectively. The red (blue) dots indicate the clouds with low (high) cloud tops, and the red (blue) line is fitted from clouds with similar cloud tops using the linear least square method. The arrow on the line indicates the increase in the cloud optical thickness. This schematic diagram was drawn based on Cess et al. (2001a, b).

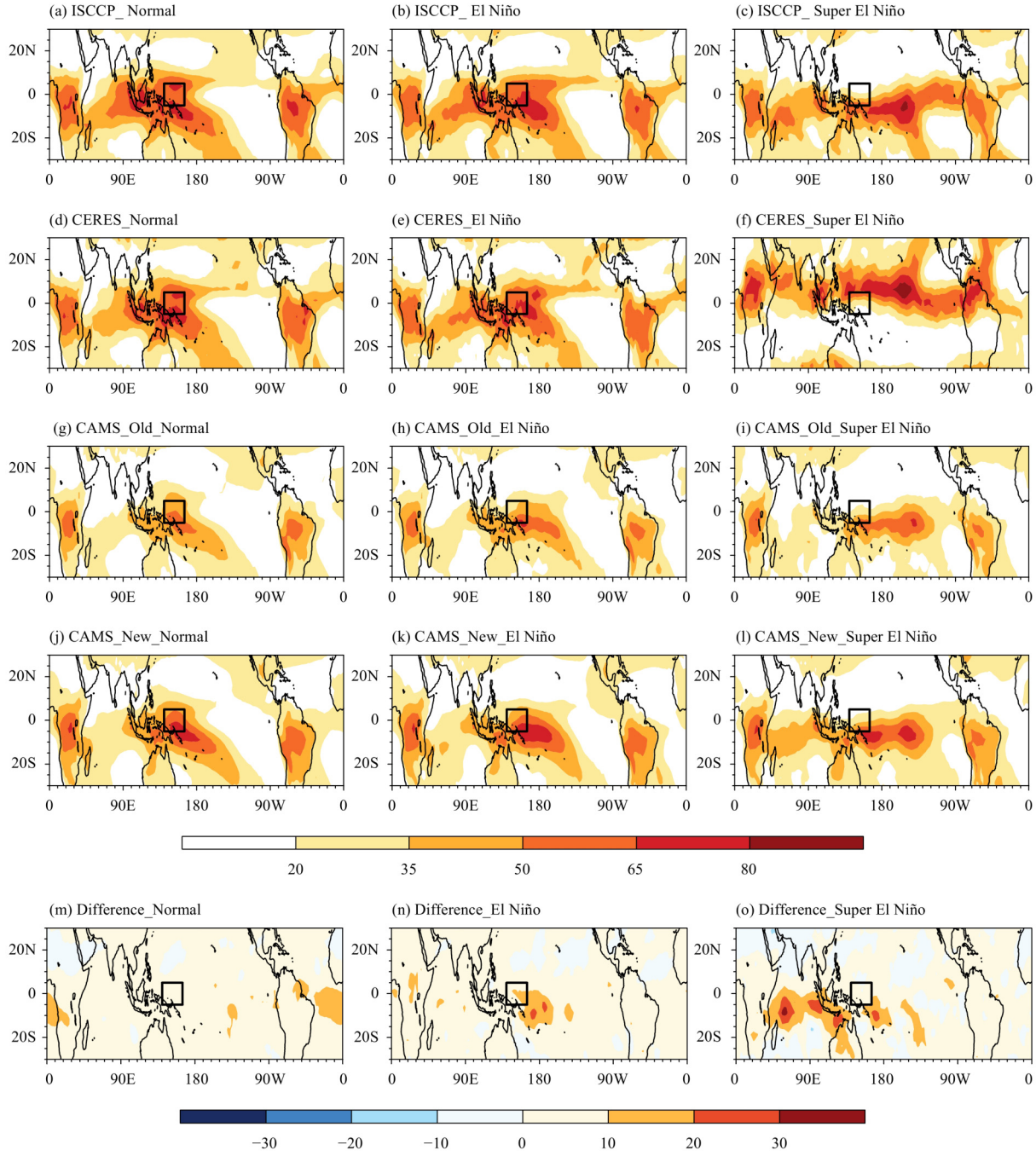

Fig. 2. Geographical distributions of JFMA (January–April) averaged LWCRF (W m^{-2}) during (a, d, g) normal years, (b, e, h) El Niño years, and (c, f, i) super El Niño years (details in Section 2.4) from (a–c) ISCCP, (d–f) CERES, (g–i) the old version of CAMS-CSM, (j–l) the new version of CAMS-CSM, and (m–o) the difference between the two versions. The black solid box denotes the warm pool (WP; 5°S–5°N, 140°–165°E).

version is improved to 29 W m^{-2}, which is closer to the observations. A similar bias is seen in SWCRF. The simulated mean SWCRF in the TP is −34 W m^{-2} in the old version and −48 W m^{-2} in the new version, in comparison with less than −55 W m^{-2} in ISCCP and −54 W m^{-2} in CERES. The biases over the WP are similar to those over the TP (Table 2). Nevertheless, both the old and new versions of CAMS-CSM can generally capture the cancellation between LWCRF and SWCRF, with a regionally averaged NETCRF of approximately 4 W m^{-2} in the old version and −5 W m^{-2} in the new version over the WP, which are close to the observed −15 W m^{-2}.

Both LWCRF and SWCRF decrease in El Niño events and especially in super El Niño events. The regional

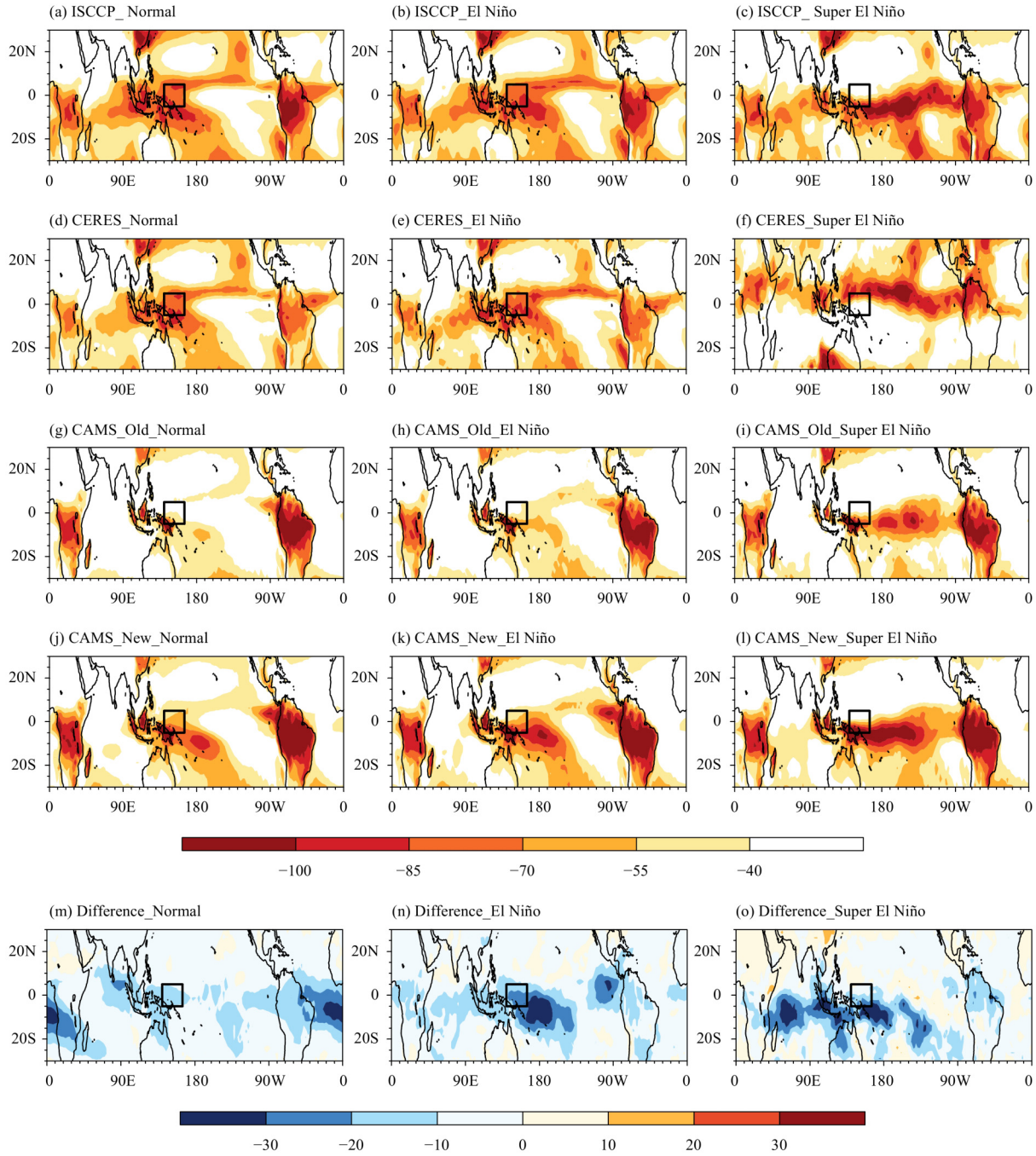

Fig. 3. As in Fig. 2, but for SWCRF.

Table 2. Mean values of LWCRF (W m^{-2}), SWCRF (W m^{-2}), and *N* with ISCCP, CERES, and CAMS-CSM over the tropical Pacific (TP; 10°S–10°N, 140°E–90°W) and warm pool (WP; 5°S–5°N, 140°–165°E) in different years

		Normal year				El Niño year				Super El Niño year			
		ISCCP	CERES	$CAMS_{Old}$	$CAMS_{New}$	ISCCP	CERES	$CAMS_{Old}$	$CAMS_{New}$	ISCCP	CERES	$CAMS_{Old}$	$CAMS_{New}$
LWCRF	TP	33	34	23	29	39	35	27	33	42	46	32	36
	WP	63	64	48	59	62	62	42	52	29	33	28	31
SWCRF	TP	−55	−54	−34	−48	−63	−57	−43	−58	−69	−64	−57	−65
	WP	−81	−81	−44	−66	−82	−81	−45	−67	−51	−46	−48	−61
N	TP	2.0	1.9	1.9	2.0	1.9	2.3	2.0	2.1	1.8	1.4	1.0	1.9
	WP	1.3	1.3	0.9	1.1	1.3	1.3	1.1	1.3	1.7	1.4	1.7	1.8

mean LWCRF over the WP is reduced from 63 to 29 W m^{-2} in ISCCP and from 64 to 33 W m^{-2} in CERES in response to a super El Niño, e.g., during 1998. Similarly, sharp decreases in SWCRF are also seen in both ISCCP (30 W m^{-2}) and CERES (35 W m^{-2}). Such responses in CRF are largely underestimated by CAMS-CSM in both the old and new versions, particularly for components of SWCRF. The simulated SWCRF response over the WP is nearly 0 W m^{-2}.

To better demonstrate the response of CRF to El Niño events, Fig. 4 compares the spatial pattern of N (N = −SWCRF/LWCRF) among different datasets. The ratio N is approximately 1.6 over the WP but exceeds 3 over the eastern Pacific (10°S–10°N, 135°–90°W; Figs. 4a–e) because of the spatial patterns of SWCRF and LWCRF. Both the old and new versions show that the simulated pattern of N is weaker than that of the observations caused by the weak SWCRF, but the value is greater than

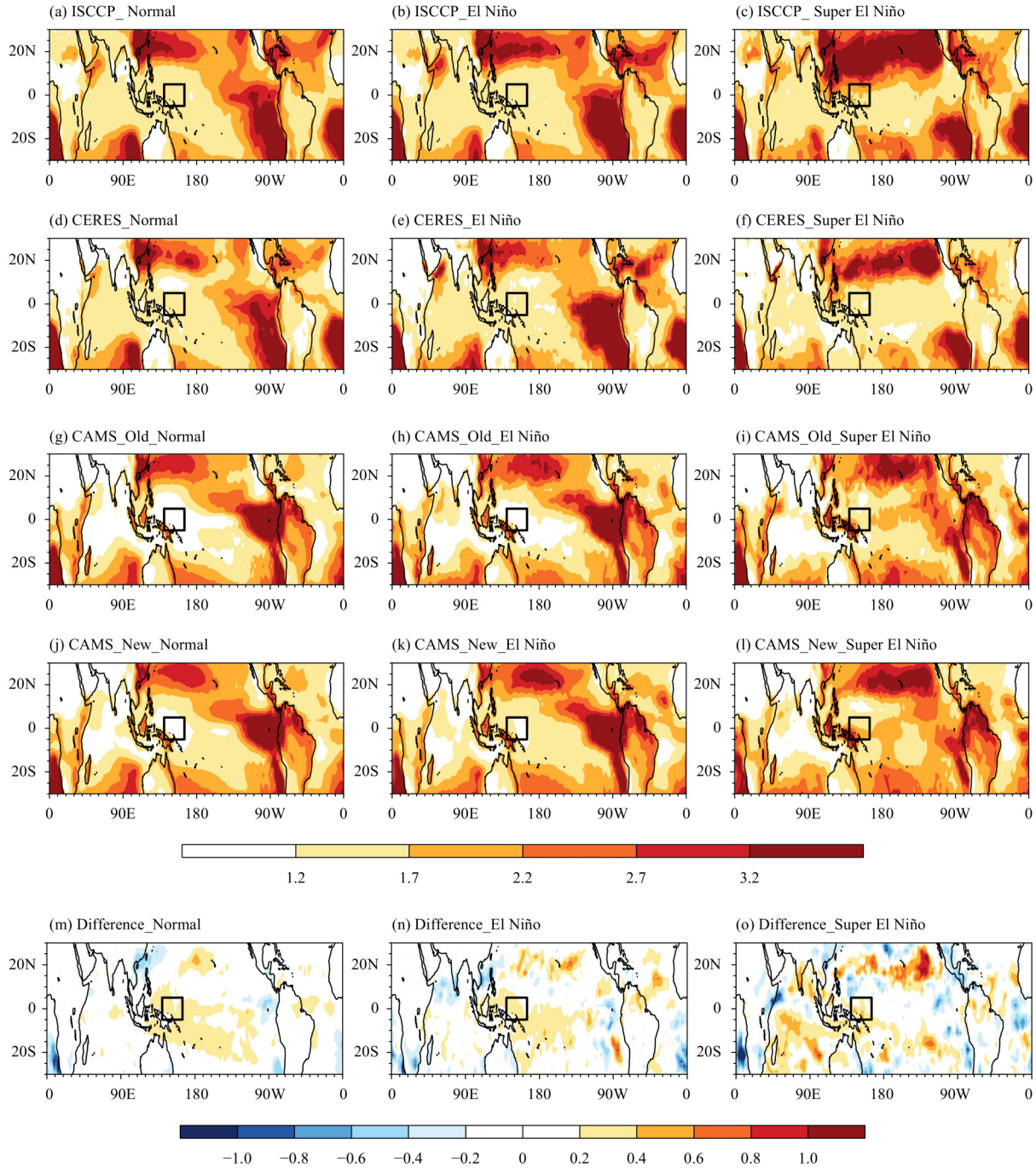

Fig. 4. As in Fig. 2, but for the CRF ratio N = −SWCRF/LWCRF.

3 over the Maritime Continent (approximately 5°S, 140°E), indicating that the model has some biases between the sea and the land.

The interannual variations in CRF and *N* over the WP from different datasets are compared in Fig. 5. Generally, CRF is weaker in the old CAMS-CSM version than in the satellite datasets, particularly for SWCRF, producing an underestimation in *N*; and the CRF and *N* biases are reduced in the new version. Moreover, the simulated interannual variations in CRF values are weaker in both the new and old versions compared to the observations. For example, SWCRF shows a change of up to 50 W m^{-2} between 1998 and 1997 in ISCCP but only a limited variation in the CAMS simulation.

To better understand the model behaviors, Fig. 6 provides the probability distribution functions (PDFs) of

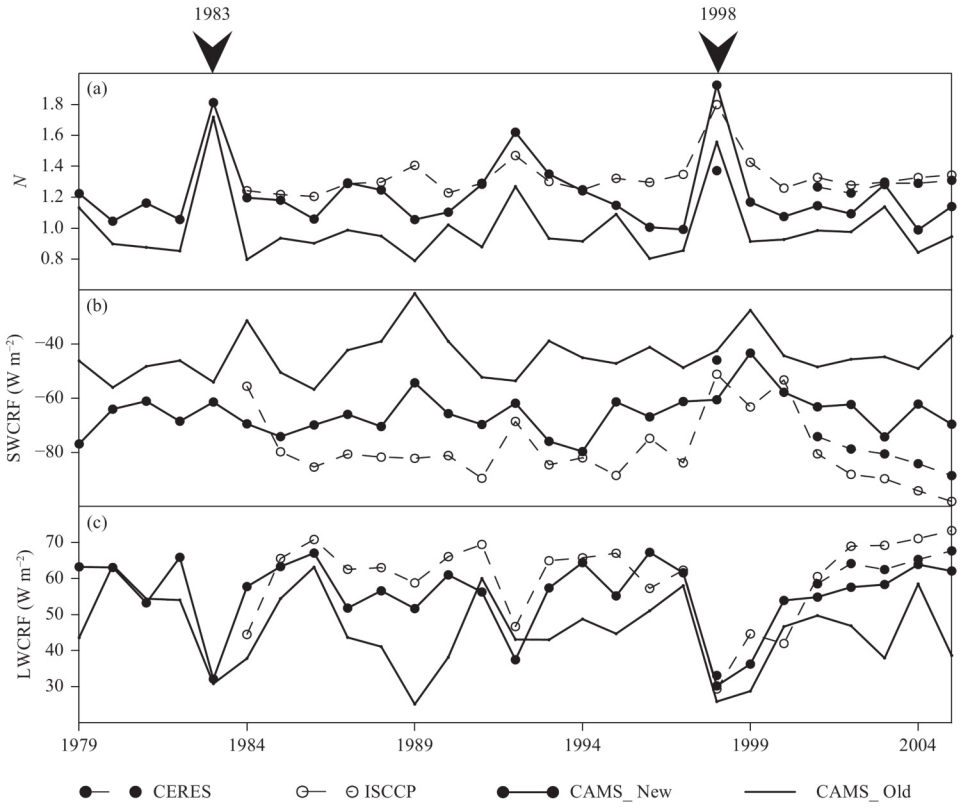

Fig. 5. Four month (JFMA) means of (a) $N = -$SWCRF/LWCRF, (b) SWCRF, and (c) LWCRF (W m^{-2}) over the WP (5°S–5°N, 140°–165°E).

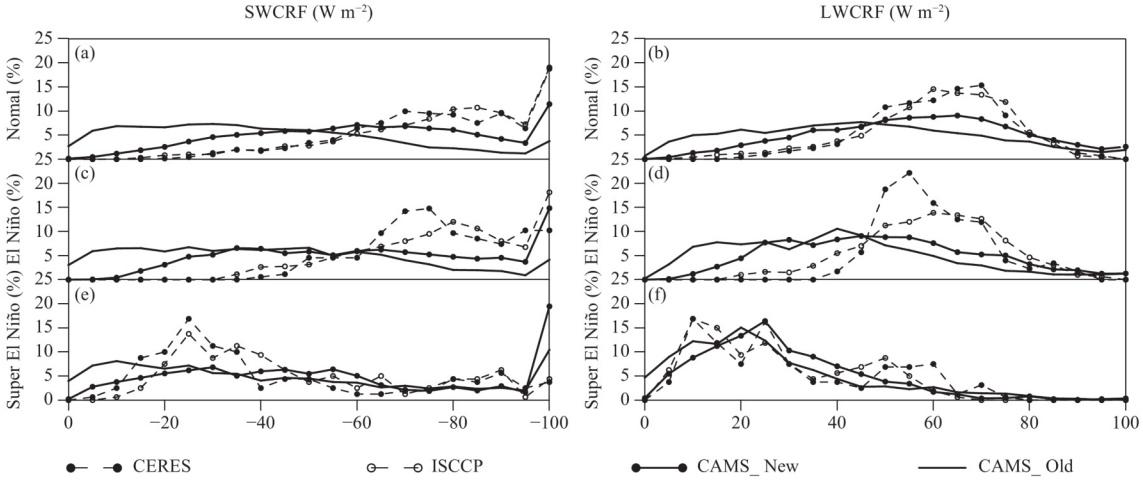

Fig. 6. Probability distribution functions (PDFs) of CRF over the WP from observations and CAMS-CSM during (a, b) normal years, (c, d) El Niño years, and (e, f) super El Niño years. (a, c, e) SWCRF and (b, d, f) LWCRF.

CRF over the WP. During normal years, the PDF peaks are populated by SWCRF at approximately −100 W m^{-2} and by LWCRF at approximately 60 W m^{-2} (Figs. 6a, b). CAMS-CSM fails to capture the observed distributions, with border shapes but lower peaks in both the SWCRF and LWCRF PDFs. During super El Niño years, the PDF peaks populated by SWCRF and LWCRF both decrease in the observations; both PDF peaks populated by SWCRF and LWCRF are approximately 40 W m^{-2}. CAMS-CSM can provide similar results for LWCRF, but its simulation skills in SWCRF are weak.

In summary, the old version of CAMS-CSM underestimates the strengths of SWCRF and LWCRF over the TP and WP, which are slightly improved in the new version. In addition, both the old and new versions of CAMS-CSM have nearly failed to reproduce the responses of CRF over the WP to the El Niño.

3.2 *Cloud properties and vertical structure over the WP*

Figure 7 shows the relationship between the NETCRF and ratio N (detailed in Section 2.5) over the WP to reveal the vertical structure of clouds. During normal years, ISCCP and CERES data show that N is linear with NETCRF. Moreover, most of the scatters appear in the area where $N < 1.3$ and NETCRF < −40 W m^{-2}, indicating that cirrus and deep convective clouds dominate over the WP (Figs. 7a, d). In the two versions of CAMS-CSM, unlike CERES, more scatters appear in the area where NETCRF exceeds −40 W m^{-2} and N exceeds 2. This indicates that the simulated cloud structure over the WP is more similar to a combination of middle-level and high clouds rather than simply deep cumulus and thin cirrus. Such a bias in cloud vertical structure can partly explain the underestimation of LWCRF during normal years (Fig. 2), as the lower averaged cloud top leads to a higher cloud brightness temperature and stronger outgoing longwave radiation.

For El Niño events, satellite data show that scatters are still distributed within the range from the bottom-right (cirrus) to the top-left quadrant (deep convective clouds). Because of the weak updrafts over the WP, however, the amount of the cirrus and deep cumulus clouds and the average cloud height over the WP decrease. The occurrence frequencies of the scatters that have $N > 1.3$ and a stronger NETCRF slightly increase. The change is more evident during the super El Niño years, in which most of the dots exceed $N = 1.3$, indicating that the proportion of middle-level clouds greatly increases (Figs. 7c, f). CAMS-CSM can capture the above observed El Niño-related cloud structure changes over the WP (Figs. 7g–i) as more dots exceed $N = 1.3$ during El Niño events. However, the simulated cloud fractions in CAMS-CSM are higher than those in the observations and the cloud heights are lower than those in the observations, which might be because of the incomplete crash of the Walker circulation during El Niño events (see Section 3.3). The cloud height is more realistic in the new version of CAMS-CSM, but the same as the old version, the cloud fractions are still larger than those in observations.

LWCRF and SWCRF are usually proportional to the cloud fractions but are exponential to the cloud optical depth or CWP. To better understand CRF in response to El Niño events, we therefore examined the simulation biases of the total cloud fraction, cloud liquid water path (LWP), and ice water path (IWP) in CAMS-CSM, as shown in Fig. 8. The average total cloud fraction is approximately 76.6% in ISCCP, 77.3% in the old version of CAMS-CSM, and 81.8% in the new version of CAMS-CSM (Fig. 8a). During El Niño events, ISCCP and CAMS-CSM both agree that the total cloud fraction shows a significant decrease because of the weak Walker circulation and its associated weak updrafts. However, the El Niño-related decrease in cloud fraction is weaker in CAMS-CSM than that in ISCCP. The biases in the updrafts are responsible, at least in part, for the underestimation of total cloud fraction changes (see Section 3.3).

Similar to the cloud fraction, the simulated CWP, defined as the sum of the cloud LWP and IWP, also shows significant decreases when El Niño events occur, which is probably the result of the weaker response of the Walker circulation to the SST changes in the model. However, the old version generally overestimates the all-year mean CWP by approximately 10 g m^{-2}, but an overestimate of nearly 70 g m^{-2} was found in the new version (Fig. 8d). We further divided the simulated CWP into the cloud LWP and the cloud IWP. It is clear that the interannual variability in the simulated CWP is mainly controlled by the cloud IWP, which decreases during El Niño events (Figs. 8b, c). The cloud LWP shows the opposite variability, which partly compensates for the negative contributions from the cloud IWP. Rather than ice clouds, liquid clouds are typically composed of small droplets and are thus efficient in light scattering. In addition, the overestimation of the cloud LWP in the new version caused by the modification of the empirical parameters may have led to the overestimation of CWP.

We therefore suspect that the responses of CRF to El Niño events are mainly dominated by the responses of the cloud vertical structure and the cloud fraction. However, the expected overestimation of SWCRF, which should be induced by the overestimation of all-year mean

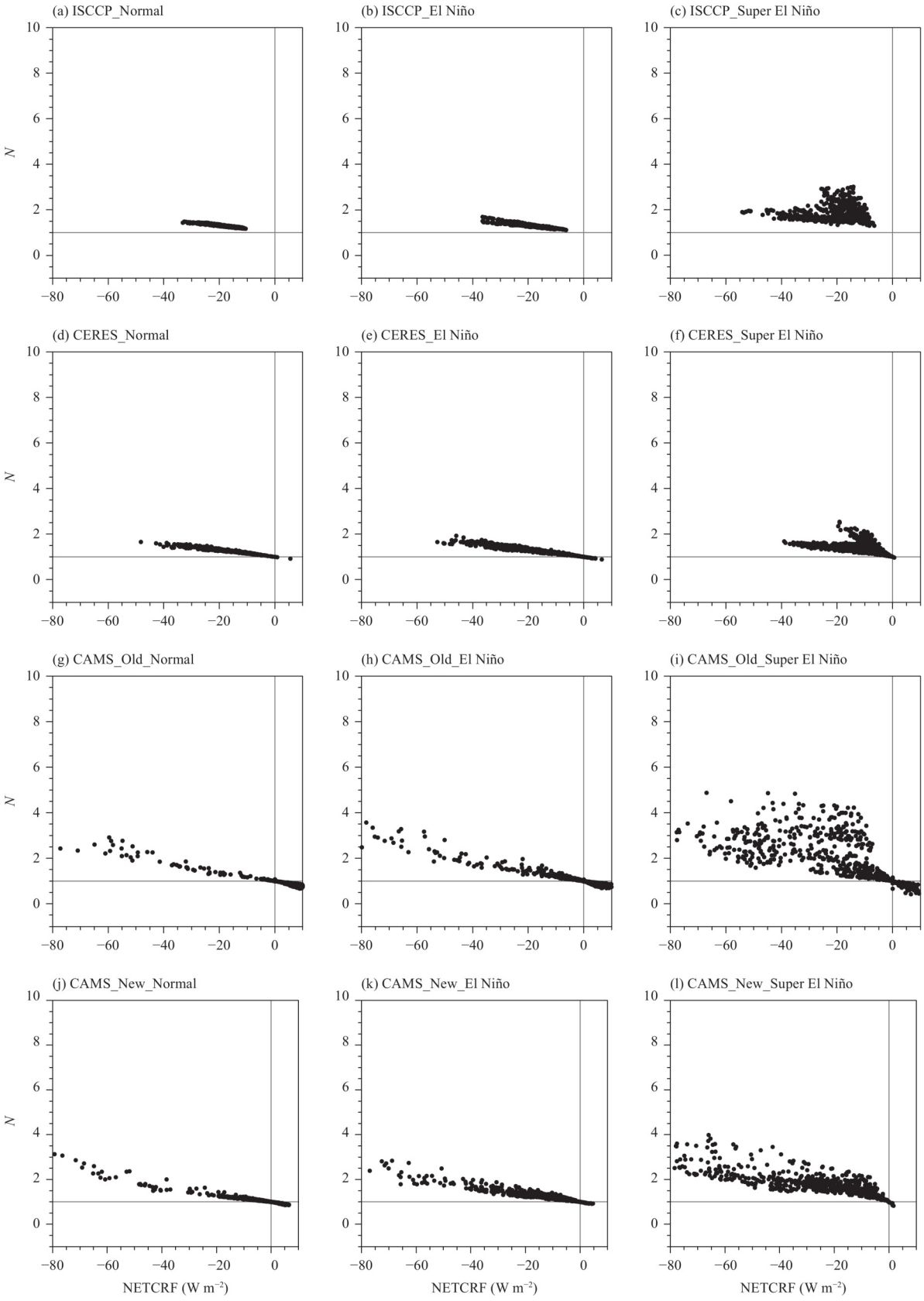

Fig. 7. Scatter plots of *N* vs. NETCRF over the WP from (a–c) ISCCP, (d–f) CERES, (g–i) old version of CAMS-CSM, and (j–l) new version of CAMS-CSM for (a, d, g, j) normal years, (b, e, h, k) El Niño years, and (c, f, i, l) super El Niño years.

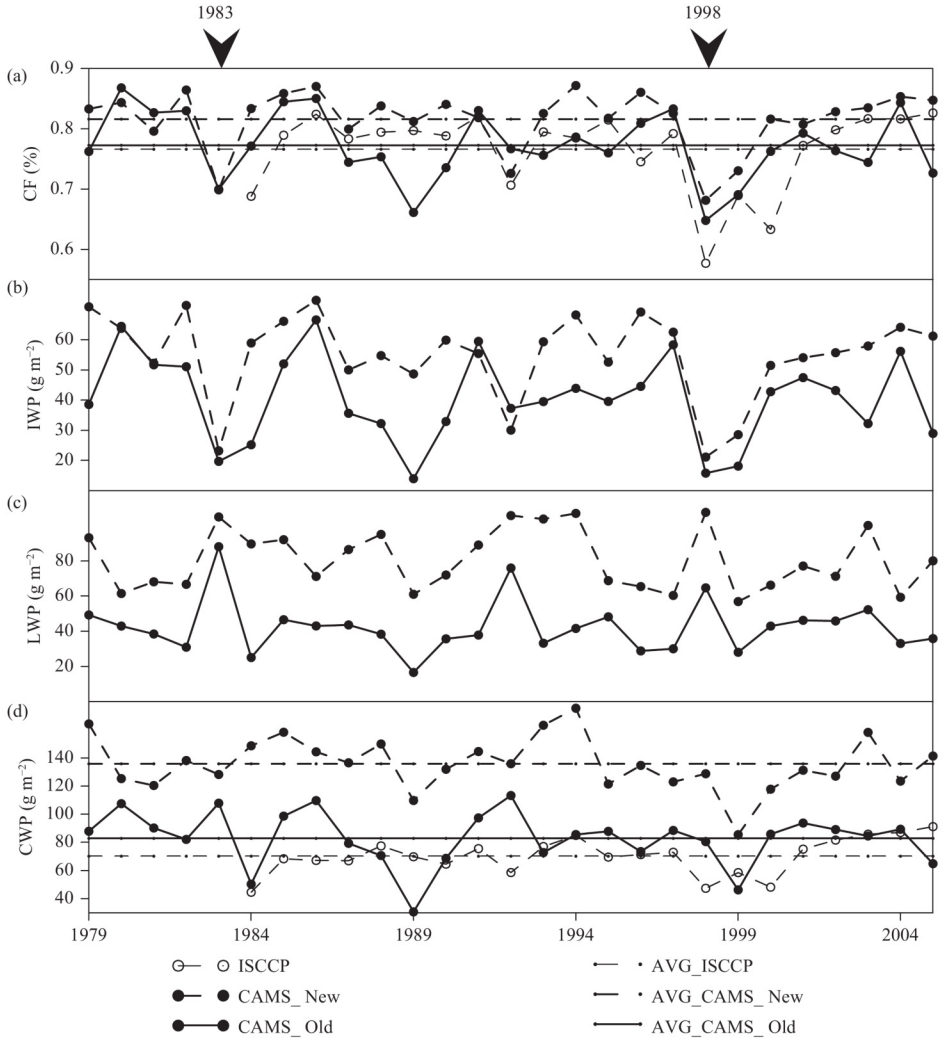

Fig. 8. Four month means (JFMA) of (a) total cloud fraction (CF), (b) ice CWP (IWP), (c) liquid CWP (LWP), and (d) CWP over the WP. The horizontal line is the mean value of different datasets.

CWP in the old version, is replaced by an underestimation, implying that other factors may compensate for or even overwhelm the effects of cloudiness and CWP in determining SWCRF, such as radiation schemes and cloud microphysics, which need discussion in the future. In the new version, even though the modification of the empirical parameters makes up the underestimation of CRF, this is the result of the overestimation of the LWP.

3.3 *Atmospheric circulation interpretation*

Previous studies have demonstrated that the variations in CRF and cloud vertical structure over the WP are highly related to the interannual variability in the Walker circulation (Cess et al., 2001a). Since the WP is underneath the updraft branch of the Walker circulation, we compared the JFMA averaged ω over the WP between the simulation and the reanalysis data. In ERA-Interim, the updraft peaks are in the middle-level troposphere (between 500 and 300 hPa) during normal years (Fig. 9a). During El Niño events, the updraft weakens because of the crash of the Walker circulation (Figs. 9b, c).

The middle-level updrafts in CAMS-CSM are stronger than those in the reanalysis in normal years, which is hardly improved in the new version. The overestimations are even more significant during the super El Niño years (Fig. 9c). For example, the simulated ω at 300 hPa is nearly four times stronger in the old version and five times stronger in the new version than that in the reanalysis. In simulations, the induced updrafts during the super El Niño years leading to the crash of the Walker circulation are incomplete and finally lead to simulated biases of the cloud vertical structure of the atmosphere. This implies that the simulated Walker circulation remains during the super El Niño years, which is inconsist-

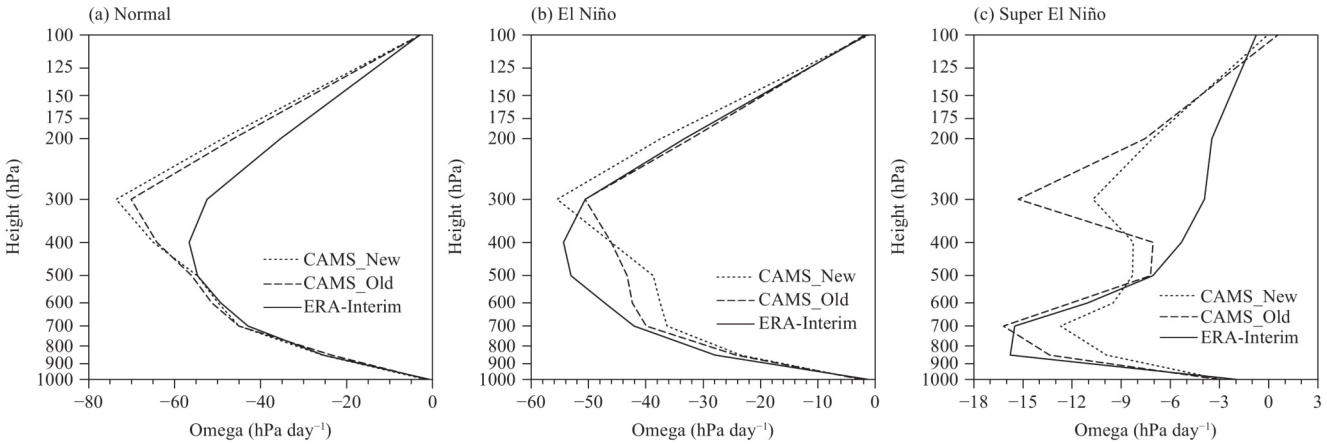

Fig. 9. Four month mean (JFMA) vertical profiles of vertical velocity (ω; hPa day^{-1}) during (a) normal years, (b) El Niño years, and (c) super El Niño years over the region (5°S–5°N, 140°–165°E) from CAMS-CSM and ERA-Interim.

ent with the situation in ERA-Interim.

To better understand the above bias, JFMA-averaged zonal winds along the equator between the simulation and the reanalysis were compared, as shown in Fig. 10. In ERA-Interim, the easterlies (westerlies) prevail in the upper part of the troposphere to the west (east) of 180°. During El Niño years, the westerlies over the WP decrease in response to the cold SST anomalies. The replacement of the westerlies by weak easterlies becomes more evident during super El Niño events (e.g., 1998). The vertical structure of the zonal winds and the weakening during El Niño events are generally reproduced in CAMS-CSM. However, biases remain evident in both the old and new versions, such as the westerlies in the upper part of the troposphere to the west of 120°W (Figs. 10f, i) in El Niño events.

We further examined the simulation biases of the mean 200-hPa velocity potential and divergent wind (Fig. 11). The simulated large-scale overturning circulations in normal years and El Niño events share some common biases. For example, the simulated tropical divergence over the WP shows an identical overestimation during each year (Figs. 11d–i). The overestimation of divergence confirms the stronger simulated updraft over the WP. Moreover, the simulated convergence over the subtropical eastern Pacific is underestimated, and the divergence over the South China Sea is weaker than that in ERA-Interim. The simulation biases can be found in both the old and new versions.

In conclusion, although the changes in empirical parameters in the new version of CAMS-CSM make some improvements to the simulation skills in CRF in normal years, biases in circulations and their induced updrafts can still be found in both the new and old versions, which can further influence the cloud vertical structure, cloud fraction, cloud water content (liquid and ice), and CRF, especially in El Niño events when the circulations over the TP are totally changed.

4. Summary

To evaluate the CAMS-CSM simulations of CRF over the WP and its responses to El Niño events, we classified years into super El Niño years, El Niño years, and normal years to compare the simulation results with the observations, and discussed the reasons for biases. The main results of this study are as follows.

(1) The mean values of SWCRF and LWCRF in CAMS-CSM are both weaker than those of the observations over the WP. The weak simulation of LWCRF was caused by the deviation in the cloud vertical structure. For example, the cloud top in CAMS-CSM was lower than that of the observation over the WP.

(2) In response to El Niño events, the simulated CRF anomalies are similar to the observations over the TP. However, focusing on the WP, the responses of LWCRF are weaker than those of the observations, and for SWCRF, CAMS-CSM cannot provide similar anomalies compared to the observations. The anomaly biases of SWCRF in CAMS-CSM are mainly caused by the incomplete shutdown of the Walker circulation during El Niño events, leading to the existence of updraft over the WP and a weaker decrease in cloud fraction, unlike the observations. For LWCRF, CAMS-CSM can provide a similar response to the observations because the cloud vertical structure response is similar to that of the observations during El Niño events. However, because of the influence of the weak response of the cloud fraction, the response of LWCRF is weaker than that of the observations.

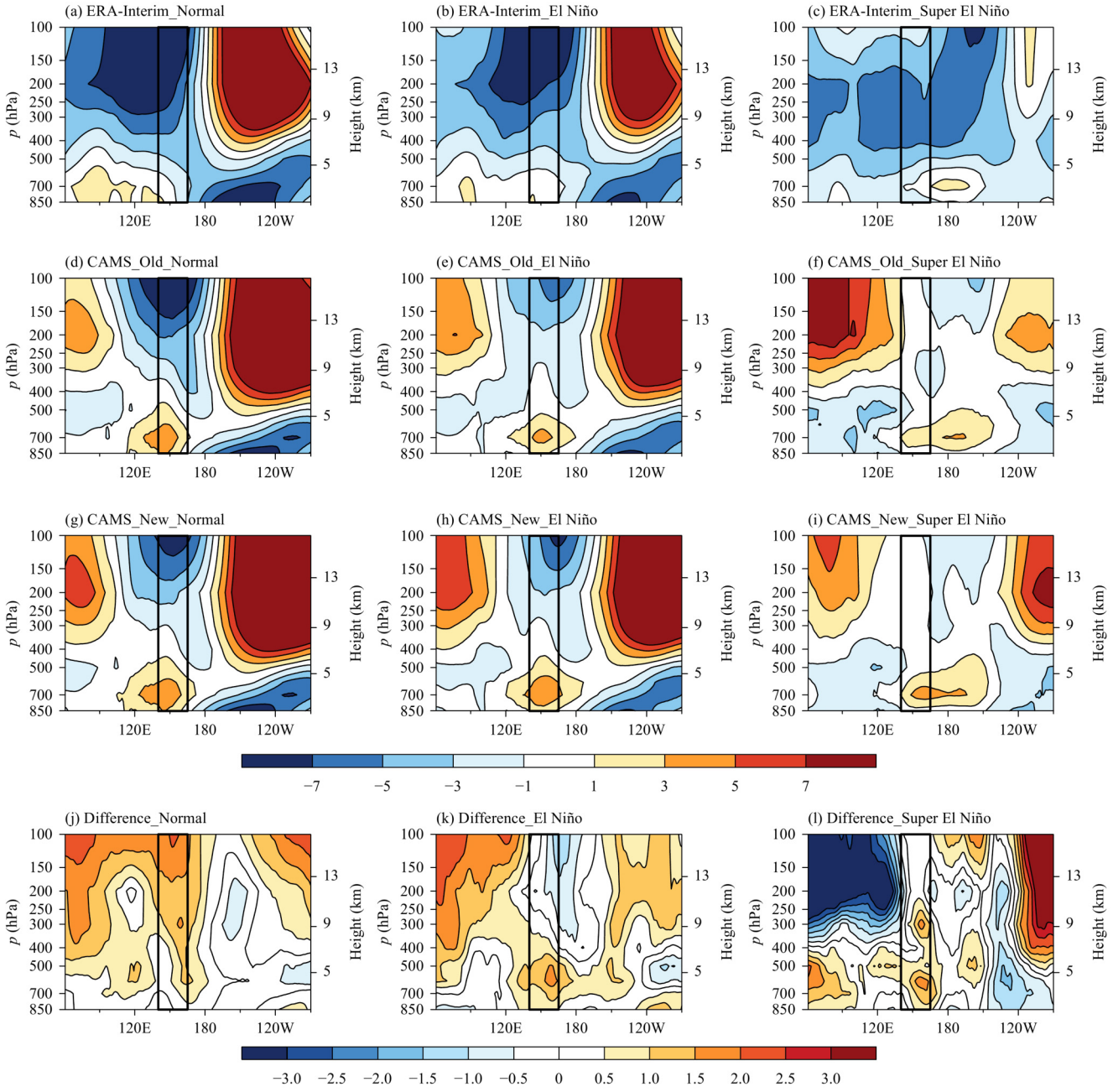

Fig. 10. JFMA mean pressure–longitude cross-sections of zonal wind (m s^{-1}) averaged from 5°S to 5°N during (a, d, g) normal years, (b, e, h) El Niño years, and (c, f, i) super El Niño years from (a–c) ERA-Interim, (d–f) old version of CAMS-CSM, (g–i) new version of CAMS-CSM, and (j–l) the difference between the two versions. The area between the black vertical solid lines is the WP (140°–165°E).

(3) The modification of the empirical parameters between the cloud droplets and the raindrops generates a realistic CRF in the new version of CAMS-CSM. The improvements in CRF are partly caused by the overestimated CWP in the new version. The simulation biases in the circulations and their induced updrafts still exist in the new version, which affect a realistic simulation of CRF responses to El Niño events. Hence, a better simulation of CRF over the WP relies heavily on the simulation of the Walker circulation.

Finally, we acknowledge that the reason for the underestimated SWCRF deserves further study. Since the value of the cloud fraction in CAMS-CSM is similar to that of the observations, the weak simulation of SWCRF is hypothesized to be related to the lower cloud molecular number concentration, which will be verified in a future study.

Acknowledgments. We thank the Chinese Academy of

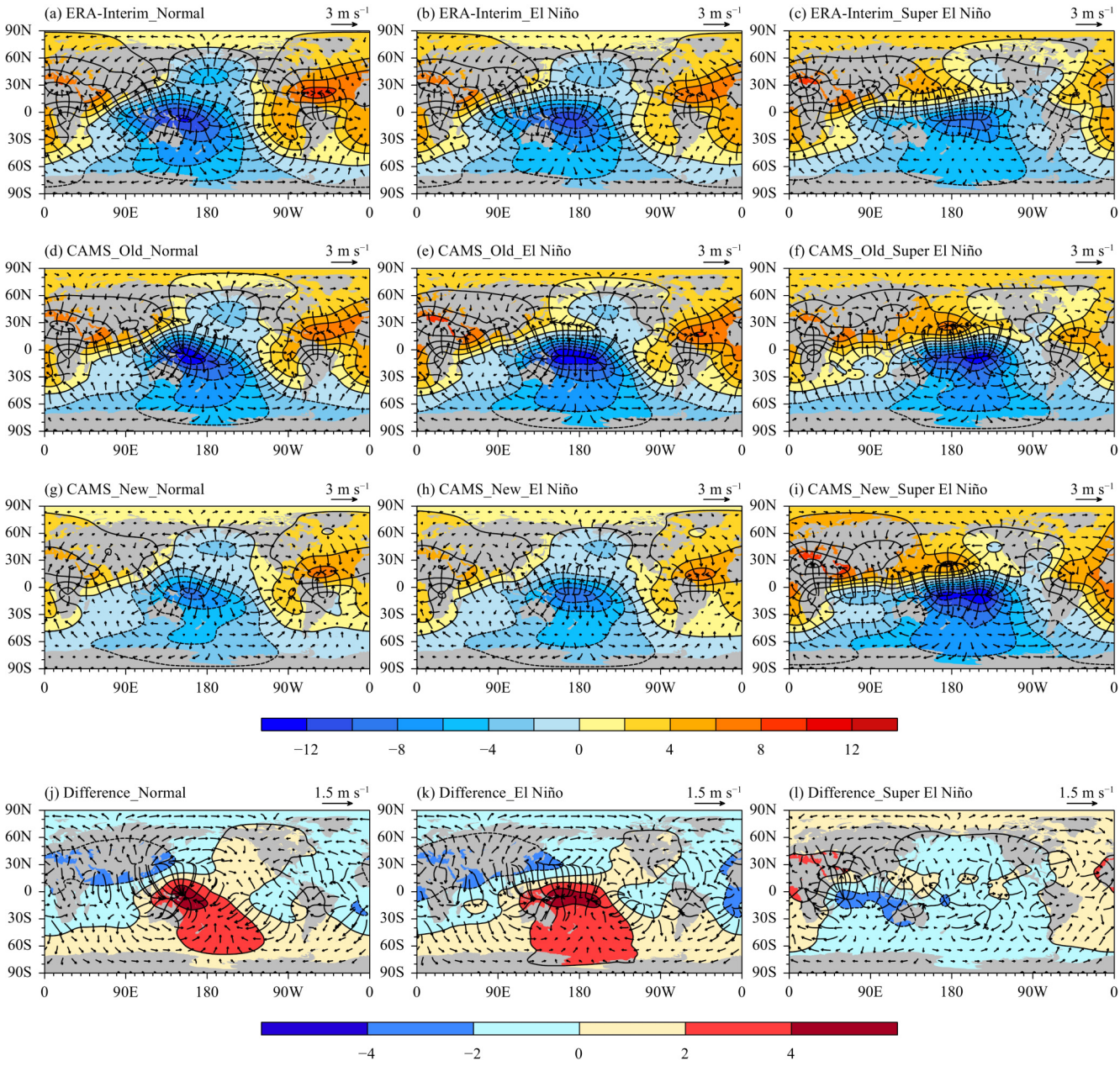

Fig. 11. JFMA mean velocity potential (10^6 m^2 s^{-1}) and divergent wind (m s^{-1}) at 200 hPa over the TP during (a, d, g) normal years, (b, e, h) El Niño years, and (c, f, i) super El Niño years from (a–c) ERA-Interim, (d–f) old version of CAMS-CSM, (g–i) new version of CAMS-CSM, and (j–l) the difference between the two versions.

Meteorological Sciences for providing the CAMS-CSM model data.

REFERENCES

Burls, N., and A. Fedorov, 2014: What controls the mean east–west sea surface temperature gradient in the equatorial Pacific: The role of cloud albedo. *J. Climate*, **27**, 2757–2778, doi: 10.1175/JCLI-D-13-00255.1.

Cess, R. D., M. H. Zhang, P.-H. Wang, et al., 2001a: Cloud structure anomalies over the tropical Pacific during the 1997/98 El Niño. *Geophys. Res. Lett.*, **28**, 4547–4550, doi: 10.1029/2001GL013750.

Cess, R. D., M. H. Zhang, B. A. Wielicki, et al., 2001b: The influence of the 1998 El Niño upon cloud-radiative forcing over the Pacific warm pool. *J. Climate*, **14**, 2129–2137, doi: 10.1175/1520-0442(2001)014<2129:TIOTEN>2.0.CO;2.

Chen, L., L. J. Hua, X. Y. Rong, et al., 2019: Cloud radiative feedbacks during the ENSO cycle simulated by CAMS-CSM. *J. Meteor. Res.*, **33**, 666–677, doi: 10.1007/s13351-019-8104-3.

Chen, T., W. B. Rossow, and Y. C. Zhang, 2000: Radiative effects of cloud-type variations. *J. Climate*, **13**, 264–286, doi: 10.1175/1520-0442(2000)013<0264:REOCTV>2.0.CO;2.

Guo, Z., and T. J. Zhou, 2012: The cloud–radiation forcing over

the western Pacific warm pool during 1997/98 simulated by two versions of LASG/IAP atmospheric general circulation model. *Chinese J. Atmos. Sci.*, **36**, 863–878, doi: 10.3878/j.issn.1006-9895.2012.11211. (in Chinese)

Harrison, E. F., P. Minnis, B. R. Barkstrom, et al., 1990: Seasonal variation of cloud radiative forcing derived from the Earth Radiation Budget Experiment. *J. Geophys. Res. Atmos.*, **95**, 18,687–18,703, doi: 10.1029/JD095iD11p18687.

Harrop, B. E., and D. L. Hartmann, 2015: The relationship between atmospheric convective radiative effect and net energy transport in the tropical warm pool. *J. Climate*, **28**, 8620–8633, doi: 10.1175/JCLI-D-15-0151.1.

Hartmann, D. L., M. E. Ockert-Bell, and M. L. Michelsen, 1992: The effect of cloud type on Earth's energy balance: Global analysis. *J. Climate*, **5**, 1281–1304, doi: 10.1175/1520-0442(1992)005<1281:TEOCTO>2.0.CO;2.

Hua, L. J., and L. Chen, 2019: ENSO asymmetry in the CAMS-CSM. *Asia-Pacific J. Atmos. Sci.*, **55**, 507–528, doi: 10.1007/s13143-018-00102-9.

Hua, L. J., L. Chen, X. Y. Rong, et al., 2019: An assessment of ENSO stability in CAMS climate system model simulations. *J. Meteor. Res.*, **33**, 80–88, doi: 10.1007/s13351-018-8092-8.

Kiehl, J. T., and V. Ramanathan, 1990: Comparison of cloud forcing derived from the Earth Radiation Budget Experiment with that simulated by the NCAR community climate model. *J. Geophys. Res. Atmos.*, **95**, 11679–11698, doi: 10.1029/JD095iD08p11679.

Kiran, V. R., M. Rajeevan, H. Gadhavi, et al., 2015: Role of vertical structure of cloud microphysical properties on cloud radiative forcing over the Asian monsoon region. *Climate Dyn.*, **45**, 3331–3345, doi: 10.1007/s00382-015-2542-0.

Lohmann, U., and E. Roeckner, 1996: Design and performance of a new cloud microphysics scheme developed for the ECHAM general circulation model. *Climate Dyn.*, **12**, 557–572, doi: 10.1007/BF00207939.

Lu, B., and H. L. Ren, 2019: ENSO features, dynamics, and teleconnections to East Asian climate as simulated in CAMS-CSM. *J. Meteor. Res.*, **33**, 46–65, doi: 10.1007/s13351-019-8101-6.

Lu, R. Y., B. W. Dong, R. D. Cess, et al., 2004: The 1997/98 El Niño: A test for climate models. *Geophys. Res. Lett.*, **31**, L12216, doi: 10.1029/2004GL019956.

Nordeng, T. E., 1994: Extended Versions of the Convective Parameterization Scheme at ECMWF and Their Impact on the Mean and Transient Activity of the Model in the Tropics. Technical Memorandum 206, ECMWF, Reading, UK, ECMWF, 41 pp.

Potter, G. L., and R. D. Cess, 2004: Testing the impact of clouds on the radiation budgets of 19 atmospheric general circulation models. *J. Geophys. Res. Atmos.*, **109**, D02106, doi: 10.1029/2003JD004018.

Roeckner, E., G. Bäuml, L. Bonaventura, et al., 2003: The Atmospheric General Circulation Model ECHAM 5. Part I: Model Description. Max-Planck-Institut für Meteorologie, 349 pp.

Rong, X. Y., J. Li, H. M. Chen, et al., 2018: The CAMS climate system model and a basic evaluation of its climatology and climate variability simulation. *J. Meteor. Res.*, **32**, 839–861, doi: 10.1007/s13351-018-8058-x.

Rossow, W. B., and R. A. Schiffer, 1991: ISCCP cloud data products. *Bull. Amer. Meteor. Soc.*, **72**, 2–20, doi: 10.1175/1520-0477(1991)072<0002:icdp>2.0.co;2 .

Simmons, A., S. Uppala, D. Dee, et al., 2006: ERA-Interim: New ECMWF Reanalysis Products from 1989 Onwards. ECMWF Newsletter 110, ECMWF, Reading, UK, 25–35.

Soden, B. J., and I. M. Held, 2006: An assessment of climate feedbacks in coupled ocean–atmosphere models. *J. Climate*, **19**, 3354–3360, doi: 10.1175/JCLI3799.1.

Sundqvist, H., 1978: A parameterization scheme for non-convective condensation including prediction of cloud water content. *Quart. J. Roy. Meteor. Soc.*, **104**, 677–690, doi: 10.1002/qj.49710444110.

Tiedtke, M., 1989: A comprehensive mass flux scheme for cumulus parameterization in large-scale models. *Mon. Wea. Rev.*, **117**, 1779–1800, doi: 10.1175/1520-0493(1989)117<1779:ACMFSF>2.0.CO;2.

Tiedtke, M., 1993: Representation of clouds in large-scale models. *Mon. Wea. Rev.*, **121**, 3040–3061, doi: 10.1175/1520-0493(1993)121<3040:ROCILS>2.0.CO;2.

Wall, C. J., D. L. Hartmann, M. M. Thieman, et al., 2018: The life cycle of anvil clouds and the top-of-atmosphere radiation balance over the tropical West Pacific. *J. Climate*, **31**, 10,059–10,080, doi: 10.1175/JCLI-D-18-0154.1.

Wang, H. L., and W. Y. Su, 2015: The ENSO effects on tropical clouds and top-of-atmosphere cloud radiative effects in CMIP5 models. *J. Geophys. Res. Atmos.*, **120**, 4443–4465, doi: 10.1002/2014JD022337.

Webb, M., C. Senior, S. Bony, et al., 2001: Combining ERBE and ISCCP data to assess clouds in the Hadley Centre, ECMWF and LMD atmospheric climate models. *Climate Dyn.*, **17**, 905–922, doi: 10.1007/s003820100157.

Webb, M. J., C. A. Senior, D. M. H. Sexton, et al., 2006: On the contribution of local feedback mechanisms to the range of climate sensitivity in two GCM ensembles. *Climate Dyn.*, **27**, 17–38, doi: 10.1007/s00382-006-0111-2.

Wielicki, B. A., B. R. Barkstrom, E. F. Harrison, et al., 1996: Clouds and the Earth's Radiant Energy System (CERES): An earth observing system experiment. *Bull. Amer. Meteor. Soc.*, **77**, 853–868, doi: 10.1175/1520-0477(1996)077<0853:catere>2.0.co;2.

Williams, K. D., and M. J. Webb, 2009: A quantitative performance assessment of cloud regimes in climate models. *Climate Dyn.*, **33**, 141–157, doi: 10.1007/s00382-008-0443-1.

Wong, T., D. F. Young, M. Haeffelin, et al., 2000: Validation of the CERES/TRMM ERBE-like monthly mean clear-sky longwave dataset and the effects of the 1998 ENSO event. *J. Climate*, **13**, 4256–4267, doi: 10.1175/1520-0442(2000)013<4256:VOTCTE>2.0.CO;2.

Wu, C. Q., T. J. Zhou, and D. Z. Sun, 2010: Regime behavior in the sea surface temperature–cloud radiative forcing relationships over the Pacific cold tongue region. *Atmos. Ocean. Sci. Lett.*, **3**, 271–276, doi: 10.1080/16742834.2010.11446881.

Wu, C. Q., T. J. Zhou, D. Z. Sun, et al., 2011: Water vapor and cloud radiative forcings over the Pacific Ocean simulated by the LASG/IAP AGCM: Sensitivity to convection schemes. *Adv. Atmos. Sci.*, **28**, 80–98, doi: 10.1007/s00376-010-9205-1.

Zhang, H., T. Nakajima, G. Y. Shi, et al., 2003: An optimal approach to overlapping bands with correlated *k* distribution method and its application to radiative calculations. *J. Geo-*

phys. Res. Atmos., **108**, 4641, doi: 10.1029/2002JD003358.

Zhang, H., G. Y. Shi, T. Nakajima, et al., 2006a: The effects of the choice of the *k*-interval number on radiative calculations. *J. Quant. Spectrosc. Radiat. Transf.*, **98**, 31–43, doi: 10.1016/j.jqsrt.2005.05.090.

Zhang, H., T. Suzuki, T. Nakajima, et al., 2006b: Effects of band division on radiative calculations. *Opt. Eng.*, **45**, 016002, doi: 10.1117/1.2160521.

Zhang, Y. C., W. B. Rossow, and A. A. Lacis, 1995: Calculation of surface and top of atmosphere radiative fluxes from physical quantities based on ISCCP data sets: 1. Method and sensitivity to input data uncertainties. *J. Geophys. Res. Atmos.*, **100**, 1149–1165, doi: 10.1029/94JD02747.

Zhang, Y. C., W. B. Rossow, A. A. Lacis, et al., 2004: Calculation of radiative fluxes from the surface to top of atmosphere based on ISCCP and other global data sets: Refinements of the radiative transfer model and the input data. *J. Geophys. Res. Atmos.*, **109**, D19105, doi: 10.1029/2003JD004457.

Tech & Copy Editor: Zhirong CHEN